Synthesis and Realizability in Design of Minimum-Simulation Inline Antenna Arrays

Matteo Oldoni, *Member, IEEE*, Stefano Moscato, Steven Caicedo Mejillones, Gian Guido Gentili, *Member, IEEE*, and Cristina D'Asta

***Abstract*— This article discusses a simplified design technique of antenna arrays. The technique relies on a single electromagnetic simulation of an arbitrary inline core element, for instance, a printed patch antenna or a waveguide slot, and several identical core elements are then cascaded by means of transmission lines with given length and characteristic impedance. Realizability constraints as well as extended possibilities are discussed. Design examples are presented and characterized for validation.**

***Index Terms*— Antenna arrays, cascade synthesis, series-fed.**

I. Introduction

In THE current landscape of wireless telecommunications, phased arrays are gradually replacing some traditional single-feed antennas, such as parabolas and horns, in several applications. Architecturally, however, phased arrays demand multiple radio frequency chains, which are unpalatable where cost, consumption, and number of components must be minimized and where dynamic beam steering is not required [1].

Single-feed arrays, on the other hand, involve one RF chain feeding a number of elements via a static distribution network, responsible for amplitude and phase at each element [2], [3]. Among these, inline antenna arrays (Fig. 1) merely require each element to be coupled with the neighboring ones, thus a more compact implementation than corporate distribution networks.

Typical practical examples include series-fed patch antennas, leaky wave antennas, and slotted waveguides.

The design of inline antenna arrays normally requires an equivalent model (i.e., a resonator), which can then be plugged into a circuit to determine the required interconnections: these techniques can be relatively simple yet powerful [4], [5]. Still relying on a simple equivalent model, other techniques require different elements along the array [6], [7], which conversely demand several separate electromagnetic simulations to dimension each element in accordance with the synthesis output. The extension to other antenna types today involves a modeling step (not trivial and implying several electromagnetic simulations) and the development of a suitable synthesis technique for the array, which, if lacking, must be replaced by several heavy electromagnetic optimizations. The principle described here derives from [8]: cascading sections all relying on the same "core" radiating element. This article provides an insightful description as well as realizability constraints and expanded possibilities, together with step-by-step examples. In detail, the proposed technique:

- requires in principle only one electromagnetic simulation of a core 2-port antenna without additional assumptions;
- allows to design with closed formulas an inline array of core elements connected by transmission lines;
- neglects mutual coupling between the radiators; crosscoupling compensation can be however applied [9];
- does not require equivalent models of the core element;
- may result in a non-uniformly spaced linear array;
- allows easy beam steering, inserting just a phase shifter between elements without redesigning the whole array.

The procedure works at a single frequency and, hence, may yield a narrowband design, but still a reasonably good starting point for optimization in case a wider bandwidth is needed.

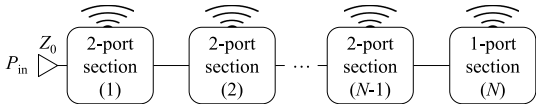

Fig. 1. Inline array: cascaded 2-port sections ended by a 1-port terminal one.

II. Basic Design Method

The main aspects of the design method are mutuated from [8], but here recalled and revised with several novel and specific insights. For simplicity, the discussion is referred to a transmitting array, while reception is obtained by reciprocity.

Remark 1: The proposed technique makes each section, at design frequency f_0 and at reference impedance Z_0:

1) matched at its input, when its output is closed on Z_0;
2) radiating an illumination-dependent fraction of the input power and forwarding the rest to the following sections;
3) provide radiation in-phase with the following sections, in a considered spatial direction.

In the following, the general nth section is designed fulfilling the three requirements above. All impedances will be normalized to Z_0 and denoted with lowercase letters.

Manuscript received 31 July 2023; revised 10 January 2024; accepted 28 January 2024. Date of publication 26 February 2024; date of current version 9 April 2024. *(Corresponding author: Matteo Oldoni.)*

Matteo Oldoni, Gian Guido Gentili, and Cristina D'Asta are with the Electronics, Information and Bioengineering Department, Politecnico di Milano, 20133 Milan, Italy (e-mail: matteo.oldoni@polimi.it).

Stefano Moscato and Steven Caicedo Mejillones are with the Research and Development Department, SIAE Microelettronica, Milan, 20093 Cologno Monzese, Italy.

Color versions of one or more figures in this article are available at https://doi.org/10.1109/TAP.2024.3366275.

Digital Object Identifier 10.1109/TAP.2024.3366275

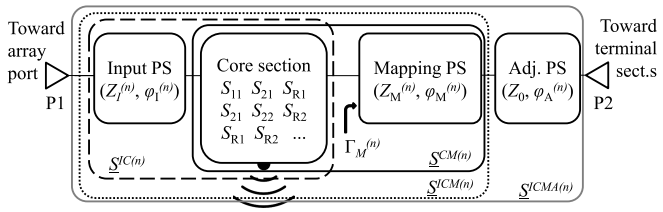

Fig. 2. Structure of section n in the array and involved scattering parameters.

The synthesis philosophy is to start from the terminal section, proceeding backward toward the feed of the array.

A. Section Structure

Each section, as shown in Fig. 2, comprises an input phase shifter (normalized impedance $z_I^{(n)}$ and electrical length $\phi_I^{(n)}$), a core radiating element, and an output network, including a "mapping" phase shifter ($z_M^{(n)}$, $\phi_M^{(n)}$) and, for all nonterminal sections, an "adjustment" phase shifter (unitary characteristic impedance, electrical length $\phi_A^{(n)}$). The core radiating element is a reciprocal 2-port antenna, with external behavior fully known via an electromagnetic simulation returning:

1) The scattering parameters referred to impedance Z_0

$$\underline{\underline{S}} = \begin{bmatrix} S_{11} & S_{21} \\ S_{21} & S_{22} \end{bmatrix}; \quad \Delta = \mathrm{Det}\left(\underline{\underline{S}}\right) = S_{11}S_{22} - S_{21}^2. \quad (1)$$

2) Radiated field in the desired spatial direction, measured at a prescribed far-field distance when fed from each of the two ports with a prescribed power P. The radiated field component is denoted as S_{R1} (when fed from port 1 with port 2 on a matched load) and as S_{R2} (when fed from port 2 with port 1 on a matched load). Only the relative phase and amplitude of S_{R1} and S_{R2} are relevant; hence, the chosen far-field distance is not influent.

All the N sections use the same core element; thus, in principle, just one electromagnetic simulation is needed for the method. Under these assumptions and feasibility constraints, in fact, the array designed by the proposed procedure will perform as intended without needing any further simulation or optimization, as discussed further in Section IV.

The phase shifters have scattering parameters given in Fig. 3 (top) and are implemented by transmission lines giving the same scattering parameters, as explained in Appendixes I and II. The mapping phase shifter can, in principle, be replaced with more complicated structures (not treated here) to overcome manufacturing constraints. The output network of the terminal section is constituted just by the mapping phase shifter, open- or short-circuited, and does not expose a second port.

B. Matched Input

According to the hypotheses, each nonterminal section is closed onto another similar section, and thus, a *divide-et-impera* choice is to impose that each section alone is matched

$$0 = S_{11}^{ICMA(n)} = S_{11}^{IC(n)} + \frac{S_{21}^{IC(n)2}\Gamma_M^{(n)}}{1 - S_{22}^{IC(n)}\Gamma_M^{(n)}} \quad (2)$$

where $\Gamma_M^{(n)}$ is the reflection observed looking into the output network closed onto a matched load, which must, thus, fulfill

$$\Gamma_M^{(n)} = \frac{S_{11}^{IC(n)}}{\mathrm{Det}\left(\underline{\underline{S}}^{IC(n)}\right)} = \frac{S_{11}^{I(n)} - \mathrm{Det}\left(\underline{\underline{S}}^{I(n)}\right)S_{11}}{S_{11}^{I(n)}S_{22} - \Delta\,\mathrm{Det}\left(\underline{\underline{S}}^{I(n)}\right)}. \quad (3)$$

For whatever choice of $z_I^{(n)}$ and $\phi_I^{(n)}$, $\underline{\underline{S}}^{IC(n)}$ can be computed as cascade of the input phase shifter and the known core (1), resulting in the needed $\Gamma_M^{(n)}$ for input matching

$$\Gamma_M^{(n)} = \frac{-2S_{11}z_I^{(n)} + j\tan\phi_I^{(n)}\left(1 + S_{11} - z_I^{(n)2}(1 - S_{11})\right)}{-2\Delta z_I^{(n)} + j\tan\phi_I^{(n)}\left(S_{22} + \Delta - z_I^{(n)2}(S_{22} - \Delta)\right)}. \quad (4)$$

The task of transforming a matched $z_0 = 1$ load at port 2 of the section into the required $\Gamma_M^{(n)}$ is demanded to the "mapping" phase shifter, as described in Section II-D. The choice of $z_I^{(n)}$ and $\phi_I^{(n)}$ is, however, constrained by the other requirements, as explained in the following.

C. Operating Power Gain

Of the requirements set out in Remark 1, the one concerning quotas of radiated and transferred power is considered now, which is directly related to the power gain of the section.

Assuming that the core network has only radiation losses, whatever power enters the network through port 1 is either radiated or transferred on to the following stages. Several illumination distributions [10] can be used, i.e., uniform, Dolph–Tchebychev, and Orchard [11], [12], [13], [14], each with different efficiencies and side lobes. The case of uniform illumination with in-phase radiation is considered for simplicity:

- The terminal section must radiate all the power it accepts.
- The last-but-one section must radiate half of the accepted power and forward the other half to the terminal section.
- In general, the nth section counted from the feed point, being the last-but-m with $m = N - n$ has

$$G_P^{(n)} = \frac{\text{Power forwarded to the following sect.}}{\text{Power accepted at its port 1}} = \frac{m}{m+1} \quad (5)$$

$$\frac{\text{Power radiated by section } n}{\text{Power accepted at its port 1}} = 1 - G_P^{(n)} = \frac{1}{m+1}. \quad (6)$$

Fig. 3 shows these formulas for a uniform array, confirming that the radiated power from each element is the same. When a nonuniform illumination $I^{(n)}$ is instead required, the power gain of each section can be computed as in Appendix II

$$G_P^{(n)} = 1 - \frac{I^{(n)}}{1 - \sum_{i<n} I^{(i)}}. \quad (7)$$

Thus, (5) or the chosen illumination distribution provides the required power gains at the beginning of the procedure for all sections $n = 1, \ldots, N$. The operating power gain [15] of a general 2-port network (whose scattering parameters are denoted as $\hat{S}_{n,m}$) is a function of the load onto which the network is closed Γ_L; hence, the notation $G_P(\Gamma_L)$

$$G_P(\Gamma_L) = \frac{\left|\hat{S}_{21}\right|^2}{1 - |\Gamma_{in}|^2}\frac{1 - |\Gamma_L|^2}{\left|1 - \hat{S}_{22}\Gamma_L\right|^2} \quad \text{with}$$

$$\Gamma_{in} = \hat{S}_{11} + \frac{\hat{S}_{21}^2\Gamma_L}{1 - \hat{S}_{22}\Gamma_L}.$$

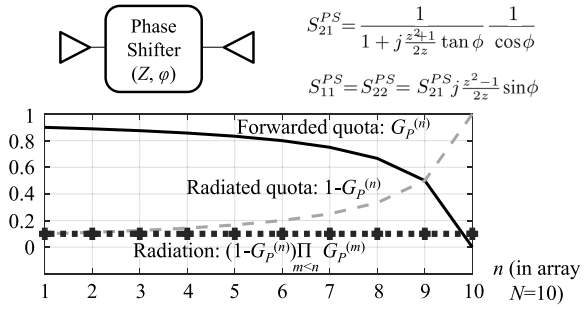

Fig. 3. Top: generic phase shifter and its scattering parameters as a function of its electrical length ϕ and normalized characteristic impedance z. Bottom: power gain (solid line) along an $N = 10$ array and its complementary radiated power fraction (dashed line) of each section for uniform illumination; actual radiated power (dotted line) from each section is proportional to the cumulative product of the power gains of the previous sections.

The overall section's operational power gain $G_P^{ICMA}(0)$, which must equal (5), is the product of the individual gains and, due to $\underline{\underline{S}}^{MA(n)}$ being lossless is, thus,

$$G_P^{ICMA(n)}(0)=G_P^{IC(n)}\left(\Gamma_M^{(n)}\right)\cdot G_P^{MA(n)}(0)=G_P^{IC(n)}\left(\Gamma_M^{(n)}\right).$$

The $\underline{\underline{S}}^{IC(n)}$ network instead is lossy seen from the two physical ports, as radiation also occurs, but it is matched at its input when closed onto $\Gamma_M^{(n)}$ of (3), and thus,

$$G_P^{IC(n)}\left(\Gamma_M^{(n)}\right)=\frac{\left|S_{21}^{IC(n)}\right|^2\left(1-\left|\Gamma_M^{(n)}\right|^2\right)}{\left|1-S_{22}^{IC(n)}\Gamma_M^{(n)}\right|^2}=\frac{\left|\Delta^{IC(n)}\right|^2-\left|S_{11}^{IC(n)}\right|^2}{\left|S_{21}^{IC(n)}\right|^2} \tag{8}$$

where the last equality is obtained by replacing (3), itself function of the $\underline{\underline{S}}^{IC(n)}$ scattering parameters. Since all of them depend on $z_I^{(n)}$ and $\phi_I^{(n)}$, as well as on the core's scattering parameters, the expression can be developed to obtain

$$\begin{aligned}G_P^{ICMA(n)}(0)&=\frac{|S_{21}|^2-1}{|S_{21}|^2}\frac{\sin^2\left(\phi_I^{(n)}\right)}{4}\left(z_I^{(n)}-\frac{1}{z_I^{(n)}}\right)^2\\&+G_C^{IC}\left(\cos^2\left(\phi_I^{(n)}\right)+\frac{\sin^2\left(\phi_I^{(n)}\right)}{4}\left(z_I^{(n)}+\frac{1}{z_I^{(n)}}\right)^2\right)\\&+\frac{\sin^2\left(\phi_I^{(n)}\right)}{2}\left(z_I^{(n)^2}-\frac{1}{z_I^{(n)^2}}\right)\frac{\mathrm{Re}(B)}{|S_{21}|^2}\\&-\cos\phi_I^{(n)}\sin\phi_I^{(n)}\left(z_I^{(n)}-\frac{1}{z_I^{(n)}}\right)\frac{\mathrm{Im}(B)}{|S_{21}|^2}\end{aligned} \tag{9}$$

of which an example is given in Fig. 4, and with

$$G_c^{IC}=\left(|\Delta|^2-|S_{11}|^2\right)/\left(|S_{21}|^2\right)\text{ and }B=S_{11}-S_{22}{}^*\Delta. \tag{10}$$

Thus, $G_P^{ICMA(n)}(0)$ is practically function of $(z_I^{(n)},\phi_I^{(n)})$, periodic in $\phi_I^{(n)}$ with period π, as observable by inspection.

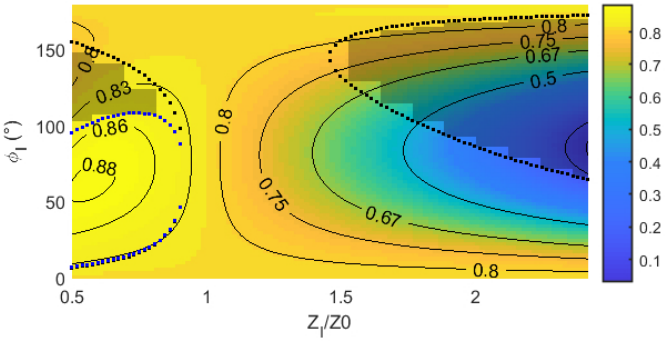

Fig. 4. Colored background: achievable operating power gain surface [(9), in linear scale] as a function of z_I and ϕ for the set of scattering parameters used in Section V-A; solid black: contour lines corresponding to the power gain values along a uniform-illumination array; gray-shaded regions with dotted boundaries: combinations of z_I and ϕ_I corresponding to a mapping network (when treating a nonterminal section) not realizable as a simple phase shifter, described in Section III-B.

For $z_I^{(n)}=1$, besides, the gain becomes independent on $\phi_I^{(n)}$ and equal to the "critical" value G_c^{IC}, with $\Gamma_M^{(n)}=S_{11}/\Delta$.

For the designer, the purpose is to identify the $(z_I^{(n)},\phi_I^{(n)})$ contours corresponding to $G_P^{ICMA(n)}(0)=G_P^{(n)}$ prescribed by the chosen illumination distribution; see (5). This can be achieved by either sweeping $z_I^{(n)}$ and $\phi_I^{(n)}$, while evaluating the $G_P^{ICMA(n)}(0)$ surface, or in closed form, as described in the following. Minimum and maximum values of the achievable operating power gain can be derived to establish the limits (see Section III). When the desired $G_P^{(n)}$ is within the achievable range, (9) can be manipulated to obtain $\phi_I^{(n)}$ as a second-order polynomial solution for each value of $z_I^{(n)}$

$$\begin{aligned}\tan\phi_I^{(n)}&=\left(-W^{(n)}\pm\sqrt{W^{(n)2}-4V^{(n)}P^{(n)}}\right)\Big/\left(2P^{(n)}\right)\\V^{(n)}&=z_I^{(n)2}\left(G_C^{IC}-G_P^{(n)}\right)|S_{21}|^2\\W^{(n)}&=\mathrm{Im}(B)z_I^{(n)}\left(1-z_I^{(n)2}\right)\\P^{(n)}&=\frac{|\Delta|^2-|S_{11}|^2+|S_{22}|^2-1}{4}\left(z_I^{(n)2}-1\right)^2\\&+\frac{\mathrm{Re}(B)\left(z_I^{(n)4}-1\right)}{2}+V^{(n)}.\end{aligned} \tag{11}$$

By any of the above methods (sweeping the surface or closed-form contours), one identifies the set of input phase shifter parameters, which fulfill the desired power gain. One pair $(z_I^{(n)},\phi_I^{(n)})$ must be selected among those. For any nonterminal section, only those achievable within the realizability constraints of the mapping network are acceptable, as outlined in Section II-D, whereas the terminal section does not impose further constraints on realizability.

D. Mapping Phase Shifter

A given pair $(z_I^{(n)},\phi_I^{(n)})$ implies the required $\Gamma_M^{(n)}$ via (4), which must be obtained by transforming the matched load $z_0=1$ through the mapping phase shifter.

For the terminal section $n=N$, the required 2-port power gain is $G_P^{ICMA(N)}(0)=G_P^N=0$ (since there are no further loads along the array), which implies that $\left|\Gamma_M^{(N)}\right|=1$. This can be easily obtained if the mapping phase shifter is simply

an open- or short-circuited stub with unitary impedance $z_M^{(N)} = 1$ and electrical length $\phi_M^{(N)}$

$$\phi_M^{(N)} = \begin{cases} -\dfrac{\angle\Gamma_M^{(N)}}{2} + N\pi, & \text{for open-circuit termination} \\ \dfrac{\pi}{2} - \dfrac{\angle\Gamma_M^{(N)}}{2} + N\pi, & \text{for short-circuit termination.} \end{cases} \tag{12}$$

In any nonterminal section $n < N$, instead, there is an adjustment phase shifter with unitary impedance, but it only introduces a phase delay and does not affect the mapping action. The derivation of the normalized mapping impedance $z_M^{(n)}$ and phase delay $\phi_M^{(n)}$ as the functions of $z_I^{(n)}$ and $\phi_I^{(n)}$ yield

$$\phi_M^{(n)} = \mathrm{Sign}\left(\tan\angle\Gamma_M^{(n)}\right)\arctan\left(\frac{\sqrt{\cos^2\left(\angle\Gamma_M^{(n)}\right) - \left|\Gamma_M^{(n)}\right|^2}}{\left|\sin\angle\Gamma_M^{(n)}\right|}\right) + N\pi$$

$$z_M^{(n)} = \sqrt{\frac{\cos\angle\Gamma_M^{(n)} + \left|\Gamma_M^{(n)}\right|}{\cos\angle\Gamma_M^{(n)} - \left|\Gamma_M^{(n)}\right|}}, \tag{13}$$

If $\left|\Gamma_M^{(n)} + 0.5\right| \le 0.5$ or $\left|\Gamma_M^{(n)} - 0.5\right| \le 0.5$. Therefore, for any candidate pair of $(z_I^{(n)}, \phi_I^{(n)})$, the required mapping phase shifter can be determined. If the obtained values are not acceptable due to manufacturing constraints, the candidate pair must be rejected or a different output network considered, for instance, a single-stub network as general solution or using Section III-C.

E. Radiated Field

The radiation from an entire nonterminal section $n < N$ can be computed considering the ($\underline{\underline{S}}^{ICMA(n)}$) network as a fictitious 3-port network where port 3 observes the radiation in the far-field point. Since port 2 is closed onto a matched load, the contribution reaching the observation point from section n is simply $S_{31}^{ICMA(n)}$: nothing is reflected at port 2; therefore, $S_{32}^{ICMA(n)}$ does not intervene. The adjustment phase shifter (itself matched yet unknown) does not affect the radiation from section n in any way, and hence, the following expressions are valid also for the terminal section ($n = N$). The radiated component is, in fact, computed by cascading the input phase shifter with the $\Gamma_M^{(n)}$-loaded core, as shown in Fig. 5

$$\begin{aligned} S_{31}^{ICMA(n)} &= S_{31}^{ICM(n)} = \frac{S_{21}^{I(n)} S_{31}^{CM(n)}}{1 - S_{22}^{I(n)} S_{11}^{CM(n)}}, \quad \text{with} \\ S_{31}^{CM(n)} &= S_{R1} + \frac{\Gamma_M^{(n)} S_{21} S_{R2}}{1 - \Gamma_M^{(n)} S_{22}} \\ S_{11}^{CM(n)} &= S_{11} + \frac{\Gamma_M^{(n)} S_{21}^2}{1 - \Gamma_M^{(n)} S_{22}}. \end{aligned} \tag{14}$$

F. Adjustment Phase Shifter (Only for Nonterminal Sections)

The adjustment phase shifter must enforce that the radiated field from the following sections, which receive the forwarded (nonradiated) power quota from section n, has the desired

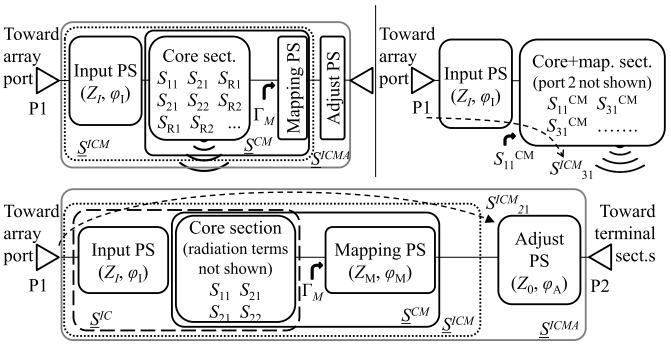

Fig. 5. Schematization of equivalent cascades used to compute scattering terms of a nonterminal section. Top: the radiation term is obtained by loading the core section with Γ_M and then cascading with the input phase shifter. Bottom: the transmission term is the forwarded contribution toward the adjustment phase shifter, hence merely the cascade of the input, core, and mapping blocks, neglecting radiation.

phase relation with the radiated field from section n. For simplicity, we assume that radiated fields must all be in phase in broadside. Radiation from section n is known via (14). The following part of the array (sections $n+1$ to N) behaves as a matched 1-port antenna, radiating with a phase delay denoted as $\angle S_{31}^{ICMA(n+1)}$ in the observation point, computable from the previous steps of the design. The adjustment shifter delays the forwarded quota, $S_{21}^{ICMA(n)}$

$$S_{21}^{ICMA(n)} = S_{21}^{ICM(n)} e^{-j\phi_A^{(n)}} \text{ with } S_{21}^{ICM(n)} = \frac{S_{21}^{IC(n)} S_{21}^{M(n)}}{1 - S_{22}^{IC(n)} S_{11}^{M(n)}} \tag{15}$$

where the ^{IC} parameters are computed by the rules of cascade

$$\begin{aligned} S_{11}^{IC(n)} &= S_{11}^{I(n)} + \frac{S_{21}^{I(n)^2} S_{11}}{1 - S_{22}^{I(n)} S_{11}}; \quad S_{21}^{IC(n)} = \frac{S_{21}^{I(n)} S_{21}}{1 - S_{22}^{I(n)} S_{11}} \\ S_{22}^{IC(n)} &= S_{22} + \frac{S_{21}{}^2 S_{22}^{I(n)}}{1 - S_{22}^{I(n)} S_{11}} \end{aligned} \tag{16}$$

and the parameters $S^{M(n)}$ of the mapping shifter follow Fig. 3. The adjustment phase shifter must, therefore, satisfy

$$\angle S_{31}^{ICM(n)} = \angle S_{21}^{ICM(n)} - \phi_A^{(n)} + \angle S_{31}^{ICMA(n+1)} \pmod{2\pi}. \tag{17}$$

For a chosen pair $(z_I^{(n)}, \phi_I^{(n)})$, finally, the adjustment phase delay must be determined to be positive with a suitable integer M, so that a physical delay line can implement it

$$\phi_A^{(n)} = \angle S_{21}^{ICM(n)} - \angle S_{31}^{ICM(n)} + \angle S_{31}^{ICMA(n+1)} + 2M\pi. \tag{18}$$

For in-phase recombination in a direction different from broadside or if a nonuniform-phase illumination is used (such as sidelobe suppression methods, such as [16] or using [9] to compensate for mutual coupling by altering phase and amplitude tapering), the adjustment phase delay determined via (18) must be altered according to the desired tilt angle from broadside and physical spacing between the elements.

The adjustment phase shifter completes the current section. The overall physical spacing between core sections is affected by the choice of ϕ_I, z_I, and therefore, different choices may lead to larger or tighter spacing. Additional $N \cdot 360°$ can moreover be added to any of the involved tx lines section, if required due to mechanical constraints or to mitigate mutual

coupling. The overall physical spacing between core sections, however, can be instead reduced, if necessary, by meandering or slow-wave lines, for instance, leveraging [17].

III. Limit Cases

The procedure outlined in Section II is, in principle, very general but might yield unacceptable results, for a given implementation technology, or not succeed at all. These limitations arise as a consequence of the absence of assumptions on the core element: for instance, one might try the technique on a very poor radiator, such as a very narrow microstrip patch, with extremely small radiation capabilities ($S_{11} = S_{22} \approx 0$, $S_{21} \approx 1$); trying to enforce (5) on the last element ($m = 0$) would fail, as the corresponding (9) could hardly be equated to 0. Intuitively, a poorly radiating element is ill-suited (e.g., requires extreme impedances) to be the core of the terminal section or of the very next sections in an array.

This depiction shows one way of failure or returning an unacceptable design. A systematic discussion of other constraints and countermeasures is presented in the following, still avoiding any further electromagnetic simulation.

A. Gain Extreme Values

The surface of $G_P^{ICMA}(0)$ as a function of $z_I^{(n)}$ and of $\phi_I^{(n)}$ exhibits maxima and minima, which may be incompatible with the values required by the illumination [e.g., (5)]. The surface can be described by contour lines, of which a parametrization has been given in (11). Some values of G_P, however, yield empty contour lines, which occur when (11) has no real solutions; the boundary between two or zero real solutions for ϕ_I occurs when the radicand is zero

$$W^2 = 4VP \;\leftrightarrow\; z_I^2\left(\alpha + \beta_I z_I^2 + \gamma_I z_I^4\right) = 0 \tag{19}$$

where the three coefficients α, β, and γ all depend on G_P

$$\begin{aligned} Z &= |\Delta|^2 - |S_{11}|^2 - |S_{22}|^2 + 1 \\ \alpha &= |S_{21}|^2\left(G_C^{IC} - G_P\right)\left(Z - 2G_C^{IC}|S_{21}|^2 + 2\,\mathrm{Re}(B)\right) + (\mathrm{Im}(B))^2 \\ \beta &= -|S_{21}|^2\left(G_C^{IC} - G_P\right)\left(Z - 2G_P|S_{21}|^2\right) - 2(\mathrm{Im}(B))^2 \\ \gamma &= |S_{21}|^2\left(G_C^{IC} - G_P\right)\left(Z - 2G_C^{IC}|S_{21}|^2 - 2\,\mathrm{Re}(B)\right) + (\mathrm{Im}(B))^2. \end{aligned}$$

For a given G_P, up to two values of z_I represent the left- and right-most extents of the contour. Such extreme values are denoted here as $z_I^E(G_P)$ and are computed as follows:

$$z_I^E(G_P) = \sqrt{\left(-\beta \pm \sqrt{\beta^2 - 4\alpha\gamma}\right)/(2\gamma)}. \tag{20}$$

If there are no real values for $z_I^E(G_P)$, the contour is empty, meaning that the surface never takes the G_P value. This happens when the outer radicand in (20) is complex, which starts to happen when the innermost radicand is zero ($\beta^2 = 4\alpha\gamma$). The condition yields the extreme value of operating power gain achievable with the chosen core section

$$G_L^P = \left(Z - \sqrt{Z^2 - 4|S_{21}|^4}\right) \Big/ \left(2|S_{21}|^2\right) \tag{21}$$

which yields a positive real result due to $\underline{\underline{S}}$ representing a strictly passive network. This limit value creates two possible ranges: $G_P < G_L^P$ or $G_P > G_L^P$. In most cases, $G_C^{IC} > 0$ and $G_C^{IC} < G_L^P$; thus, the achievable gain is determined by the first range: $0 < G_P < G_L^P$.

If the illumination function requires values beyond these limits, the core element must be altered. However, bounds on the practically acceptable values of impedance for the input phase shifter might further restrict the range of attainable gain.

B. Realizability of Mapping Phase Shifter

Once a pair $z_I^{(n)}, \phi_I^{(n)}$ has been selected to provide the gain required by the current stage, the corresponding needed reflection coefficient $\Gamma_M^{(n)}$ at port 2 of the core element is known. While other mapping structures (mentioned in Section III-C) do not impose restrictions, if this task is to be accomplished by a simple phase shifter, certain constraints apply.

Equation (13) introduces the formulas for computing the needed impedance $z_M^{(n)}$ and electrical phase delay $\phi_M^{(n)}$, with the condition for physical realizability. The condition can be depicted by Γ_M belonging to one of two 0.25-radius circles in the complex plane. These two circular regions for Γ_M must then be converted back to a condition on z_I, ϕ_I, so that realizability boundaries can be drawn together with the constant gain contours, as done in Fig. 4. The boundaries are described by the real solutions (up to 4) for every value of z_I

$$\begin{aligned} \tan\phi_I &= \frac{-b \pm \sqrt{b^2 - 4ac}}{2a} \text{ with } c = 4z_I^2\left(|S_{11}|^2 \mp \mathrm{Re}\left(S_{11}{}^*\Delta\right)\right) \\ b &= -4z_I\left(1 - z_I^2\right)\mathrm{Im}\left(S_{11} \pm S_{11}{}^*S_{22} \mp \Delta\right) \\ a &= \left(1 + z_I^2\right)^2\left(|S_{11}|^2 \mp 2\,\mathrm{Re}\left(S_{11}{}^*\Delta\right)\right) \\ &\quad + \left(1 - z_I^4\right)\mathrm{Re}\left(2S_{11} \mp S_{11}{}^*S_{22} \mp \Delta\right) \\ &\quad + \left(1 - z_I^2\right)^2(1 \mp 2\,\mathrm{Re}(S_{22})). \end{aligned} \tag{22}$$

The region (inner or outer with respect to this boundary), which contains the $z_I = 1$ axis, is the acceptable one, if $|S_{11}/\Delta + 0.5| \le 0.5 \vee |S_{11}/\Delta - 0.5| \le 0.5$.

C. Countermeasures

An arbitrary core element might prevent some steps of the synthesis from succeeding do to a few occurrences:

1) All candidate pairs z_I, ϕ_I fulfilling the required operating power gain would require unacceptable z_M impedances.
2) The required power gain can only be obtained by unacceptable z_I impedances for the input phase shifter.
3) The required operating power gain at step n is beyond the limit values of achievable gain of (21).

To tackle the first case, one can simply draw the z_I, ϕ_I contour for the needed value of operating power gain according to (11) and superimpose the boundary determining physical realizability of the mapping phase shifter (22), as done in Fig. 4. Based on these limits, it is immediate to identify what pairs of z_I and ϕ_I yield a realizable mapping phase shifter and select one as appropriate. In case the whole operating-power-gain contour does not cross the physically realizable-mapping boundary, then the whole contour is either acceptable or not.

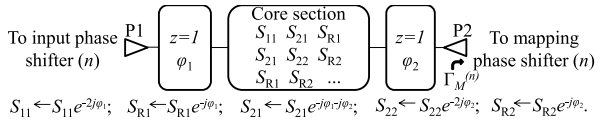

Fig. 6. Additional delays on the core element and modified parameters.

When there are no acceptable pairs, however, a possible countermeasure is to introduce a phase delay ϕ_2 on port 2 of the core element ($S_{22} \leftarrow S_{22}e^{-2j\phi_2}$, $S_{21} \leftarrow S_{21}e^{-j\phi_2}$, and $S_{R2} \leftarrow S_{R2}e^{-j\phi_2}$). This addition amounts to inserting a $z = 1$ matched transmission line section (Fig. 6) to the core element and changes the boundary of (22) for physical realizability of the phase shifter. This can similarly be seen as presenting the same required Γ_M to the original core section, but implementing it by means of two phase shifters: one with unitary normalized characteristic impedance to rotate Γ_M and one nonunitary to complete the mapping function, which always provides a solution. Other options can be similarly devised for implementing the impedance mapping with different structures, i.e., a single-stub network.

The very same approach can be considered also for tackling the other two failures. If the required operating gain contour demands unacceptable z_I, an additional phase delay (unitary-impedance transmission line section) on port 2 of the core does alter neither the operating power gain surface (9) nor its contour lines (11). Conversely, an additional phase delay ϕ_1 on port 1 of the core element ($S_{11} \leftarrow S_{11}e^{-2j\phi_1}$, $S_{21} \leftarrow S_{21}e^{-j\phi_1}$, and $S_{R1} \leftarrow S_{R1}e^{-j\phi_1}$) does alter the operating power gain surface and, hence, the available z_I, ϕ_I contour pairs and the corresponding mapping phase shifter. This countermeasure, however, can only help limitedly, since just the B quantities in (9) are affected in the gain surface, and the gain bounds of (21) still remain. An additional delay ϕ_1 is not, thus, sufficient to address the third failure possibility: in these cases, a different core element must be chosen, although possibly only in the unrealizable sections of the array.

IV. Practical Procedure

The design procedure, under the assumption of maximizing broadside radiation for an array of N elements, requires knowledge of the desired illumination distribution along the array $G_P^{(n)}$ for $n = 1$ to N, e.g., using (5) for uniform illumination. Electromagnetic data of the 2-port antenna core element must be known, described by S_{11}, S_{21}, and S_{22} and the radiated field in the observation point, expressed as S_{R1} and S_{R2}, whose absolute magnitude and phases are irrelevant. The procedure, sketched in Fig. 7, provides the inline antenna array as cascade of core elements with interconnecting phase shifters, i.e., transmission line sections of different characteristic impedances. Parasitic reactive effects due to abrupt impedance changes can be compensated by using equivalent circuits, available in the literature for several implementations, e.g., rectangular waveguide discontinuities and microstrip lines. As visible, no electromagnetic simulation or optimization of the whole array is needed. However, if the feasibility constraints are not fulfilled (e.g., impedances are beyond manufacturable limit), then circuit and/or electromagnetic optimization would be needed. Similarly, if additional requirements, such as bandwidth or squint limits, are introduced, the final array should be optimized, although using the design result as good initial point. When losses are not negligible, for instance, when using low-quality substrates or conductors and especially at mm-wave frequencies, each section will dissipate; therefore, a fraction of power will neither be radiated nor forwarded to the following sections. Based on this, the power gains of each section at design time should be increased slightly. For example, for uniform illumination in a two-element array where both sections loose about 1 dB, the power gain of the last-but-one should be increased to −2.6 dB, instead of the theoretical −3 dB. The precise amount of correction, however, strictly depends on which elements introduce losses and a rigorous treatment is very difficult.

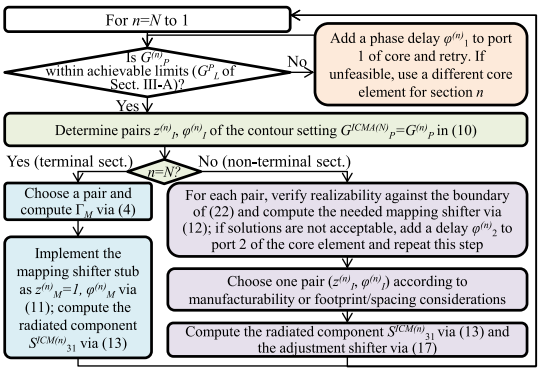

Fig. 7. Practical flowchart for inline antenna array design.

V. Examples

This section presents manufactured examples, all dedicated to broadside microstrip arrays involving uniform illumination, for simplicity, and to prove the design extensibility. The first example is a step-by-step demonstration of the procedure to $N = 4$ elements at 21 GHz. The second instead proves the extensibility of the previous array to a longer one. The last example investigates the 31-GHz empirical prototype of [8], using the improvements presented here.

A. 4 × 4 Patch Array at 21 GHz

A simple patch has been designed according to the basic design formulas [10] applied to a Rogers 4350B substrate 10-mil thick. The by-the-book unoptimized layout is shown in Fig. 8, with a 35-μm-thick copper for the patch and two $Z_0 = 50$-Ω feedlines. Reasonable impedances achievable with this technology are between 25 Ω $= 0.5Z_0$ and 120 Ω $= 2.4Z_0$.

1) Simulation: The patch with the two feedlines is modeled in Ansys Electronics Desktop. Both ports are set up to have the electric field directed from ground toward the trace at the center of the feedline, and reference planes deembedded up to the recessed feedpoints. The far-field observation point is placed in far-field at 14 000λ (corresponding to 200 m) on top of the patch, to sample electric field along the polarization axis. The 3-D simulation is run with a tight convergence requirement, since the whole array will be designed based on this single simulation. The simulated behavior is shown in

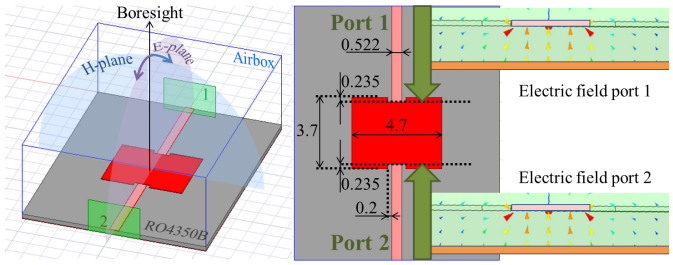

Fig. 8. Base element for 21-GHz examples of Sections V-A and V-B. The bottom wall is modeled as infinite copper ground plane. The top view shows the reference planes where the scattering parameters are computed and the electric field mode polarity of the two ports.

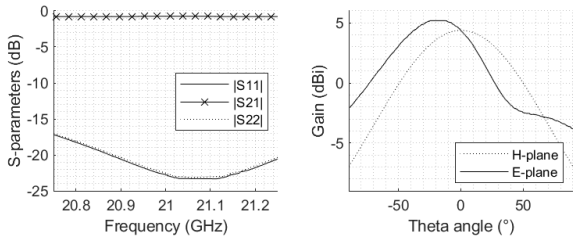

Fig. 9. Base element for 21-GHz examples: simulated scattering parameters versus frequency and gain patterns along E- and H-plane cuts at 21 GHz. Only values at boresight and at 21 GHz are used for the synthesis technique.

Fig. 9, although not strictly needed for the design procedure: reasonable matching and a slightly asymmetry in the H-plane cut, due to the nonoptimized design of the base element. Relevant to the array synthesis, instead, are the scattering parameters at 21 GHz and the polarized field component in the observation point when fed alternatively with 1 W from port 1 (giving 26.1 mV/m with phase 174°, while port 2 is closed onto a 50-Ω load) and from port 2 (26.1 mV/m with phase 354°, while port 1 is closed onto a 50-Ω load), normalized to the former

$$S_{11} = -0.05382 + j0.05101; \quad S_{22} = -0.05201 + j0.05056$$
$$S_{21} = -0.85484 + j0.31274; \quad S_{R1} = 1\angle 0°; \quad S_{R2} = 1\angle 180°.$$

2) Considerations: The considered core element creates the G_P surface of Fig. 4, evaluated via (9). The operating gain for $z_I = 1$ is $G_C^{IC} = 0.8147$, from (10). The achievable power gain, via (21), is bound to be within 0 and 0.884, making this core element good for $N < 9$ arrays (which need to radiate significantly via each section) and poor for $N \geq 10$ (whose initial sections radiate very little, as visible in Fig. 3).

To verify this intuition, a few contour lines can be drawn using (11): specifically, the figure shows the contour lines corresponding to the power gains, which are needed along a uniform-illumination array, following (5), confirming the computed bounds. By further inspection via (11), a 0 power gain can be obtained with $z_I > 2.46$ or $z_I < 0.17$, although both values are unfeasible with the chosen technology.

3) Terminal Section: The terminal section should exhibit a null power gain, but, as shown, this requires unacceptably high or low impedances for the input phase shifter. However, the choice $z_I^{(N)} = 2.4$ and $\phi_I^{(N)} = 81°$ gives a gain of 0.038 (−14.2 dB), which is acceptably close to the ideal 0. With this choice of input phase shifter for the terminal section, (4) can

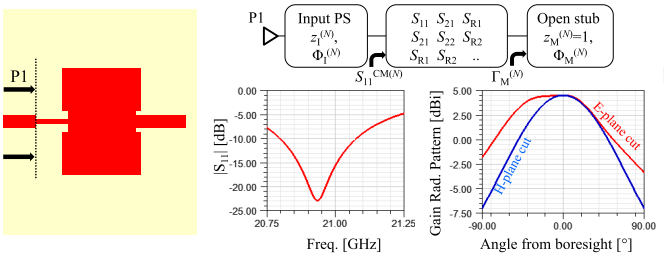

Fig. 10. Terminal section using the 21-GHz core element of Section V-A1. An additional 50-Ω line is added as input, though entirely numerically de-embedded. Equivalent model and simulated performance are also shown.

be used, which yields the supposedly unimodular reflection coefficient $\Gamma_M^{(N)} = 0.987\angle 29.9°$. Approximately, however, the output section can still be an open-circuited stub with $z_M^{(N)} = 1$ and electrical length obtained by (12) as $\phi_M^{(N)} = 165°$. The nonrealizability region for the mapping phase shifter (gray in Fig. 4) does not apply to the terminal section. The radiated field can be computed via (14) as $S_{31}^{ICMA(N)} = 2.58\angle -79°$: values larger than unity can happen due to normalization.

Only for demonstration purposes, the obtained terminal section can be simulated (Fig. 10). Due to the series reactances created at impedance discontinuities [18], a high-impedance phase shifter enclosed between two 50-Ω wider traces is altered. Proper compensation of such effects can be computed: applied to the 120-Ω input line with an ideal electrical length of 81° enclosed between 50-Ω interfaces (port 1 of the core, and section's port 1), formulas suggest that the physical line should actually be 118 Ω and 75° long, as simulated in Fig. 10.

4) $N-1$ Section: The last-but-one section in a uniform-illumination array must exhibit an operating power gain $G_P^{N-1} = 0.5$ (−3 dB). The corresponding contour in Fig. 4 is within the achievable gain limits; however, as a nonterminal section, the realizability region of the mapping phase shifter (the shaded gray area in the figure) is here relevant. In this case, we chose $z_I^{(N-1)} = 2.04$ and $\phi_I^{(N-1)} = 47°$, which requires $\Gamma_M^{(N-1)} = 0.714\angle 0.8°$. The choice results from sampling a few pairs on the contour and within the realizability region of the mapping phase shifter and selecting the one corresponding to the most realizable mapping impedance applying (13) at every sample. The obtained mapping phase shifter in the chosen point is $z_M^{(N-1)} = 120$ Ω and $\phi_M^{(N-1)} = 85°$.

Radiation from the current section is predicted by (14) as $S_{31}^{ICMA(N-1)} = 1.85\angle -60°$. The transmission through section $N-1$, except for the adjustment shifter, is computed by (15) and found to be $S_{21}^{ICM(N-1)} = 0.707\angle 19°$. Thus, the adjustment phase shifter must properly delay the forwarded portion to match the −60° from the $N-1$ section, thus fulfilling (18) to give $\phi_A^{(N-1)} = 0.3°$.

5) $N-2$ and $N-3$ Sections: To complete the four-element array, we apply the same steps of Section V-A4 twice more. The $N-2$th section must implement an operating power gain of $G_P^{(N-2)} = 0.67$ (−1.7 dB); thus, the contour available in Fig. 4 is even larger. For realizability of the mapping phase shifter, the input shifter is selected as far as possible from the boundary: $z_I^{(N-2)} = 1.6$ and $\phi_I^{(N-2)} = 41°$. The corresponding needed reflection coefficient is $\Gamma_M^{(N-2)} = 0.5\angle -6°$ from (3),

and the mapping phase shifter is $z_M^{(N-2)} = 1.7$ and $\phi_M^{(N-2)} = 97°$ by means of (13). Via (14), the radiated contribution is $S_{31}^{ICMA(N-2)} = 1.5\angle -52°$. By (15), the forwarded quota is instead $S_{21}^{ICMA(N-2)} = 0.816\angle 20°$, from which (18) is used to give the adjustment $\phi_A^{(N-1)} = 12°$.

The last section needed for this four-element array must provide an operating power gain of $G_P^{N-3} = 0.75$ (−1.25 dB). The chosen input phase shifter is $z_I^{(N-3)} = 1.25$ and $\phi_I^{(N-3)} = 47°$, needing then $\Gamma_M^{(N-3)} = 0.31\angle -4°$. The mapping phase shifter is $z_M^{(N-3)} = 1.35$ and $\phi_M^{(N-3)} = 94°$, and the final adjustment phase shifter needed is $\phi_A^{(N-3)} = 20°$.

6) Manufactured 4 × 4 Array: The 4 × 1 inline array synthesized in Section V-A5 is then parallelized to obtain a 15-dBi 4 × 4 array. The feeding network uses two-way splitters, designed independently and providing a 20-dB return loss and less than 0.5 dB of insertion loss each. The manufactured sample, equipped with an MMPX connector, is shown in Fig. 11, with simulated and measured performance. Specifically, simulations are carried out for the full electromagnetic layout and also for the ideal array: the former exactly reflects the designed layout, whereas the latter is obtained as computation of the ideal array factor applied to an array of terminal sections, used as a reference of the theoretical uniform illumination.

Electromagnetic simulations of the full array predict the return loss peak at 21.07 GHz, whereas the measurement shows it at 21 GHz, as intended. Such shift is anyway well within usual inaccuracies and fabrication spread and tolerance.

The overall array gain in boresight in the approximate array simulation predicts optimistically 16.2 dBi, neglecting all distribution losses (about 1 dB) and undesired couplings. The full electromagnetic simulation instead predicts 15.1 dBi at 21 GHz, while the measured peak gain is between 13.8 and 14.8 dBi. Such uncertainty, due to a spurious reflection in the anechoic chamber during the gain measurements (not present during radiation pattern cuts) unfortunately spotted when the chamber was no longer available, indicates some unexpected loss, possibly due to the uncalibrated connector and transition.

The normalized radiation patterns, measured and simulated by full electromagnetic simulation, instead agree very well in the E-plane, whereas the approximated array simulation again optimistically predicts lower and symmetrical sidelobes, neglecting the effect of the binary division tree on one side. The H-plane cut also shows a very good respondence in terms of sidelobe levels, although with minor differences in the notches angles between the full electromagnetic simulation and measurement. These can be ascribed to typical fabrication inaccuracies as well as imperfections of the simulation model, for instance, due to the simple first-order radiation boundary used. Overall, the agreement between measured and expected behavior (either as approximate array simulation or full array simulation) is rather good, especially without optimization.

B. 8 × 1 Patch Array at 21 GHz

The example of Section V-A successfully synthesized a 4 × 1 array with uniform illumination and radiating in broadside. The proposed technique, in case of uniform illumination,

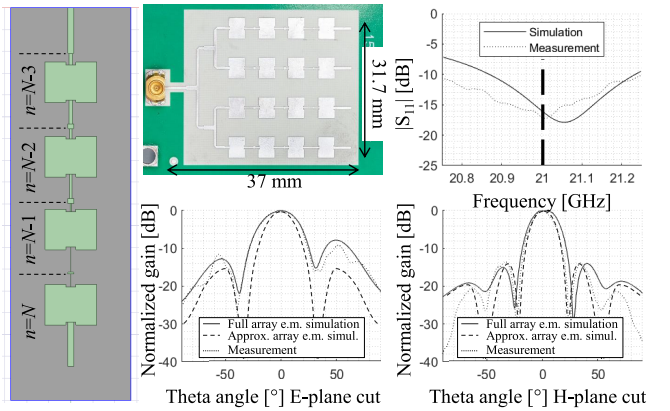

Fig. 11. Designed 4 × 1 inline array, replicated to a 4 × 4. Simulated, measured $|S_{11}|$, and normalized radiation pattern at 21 GHz is for the 4 × 4 array.

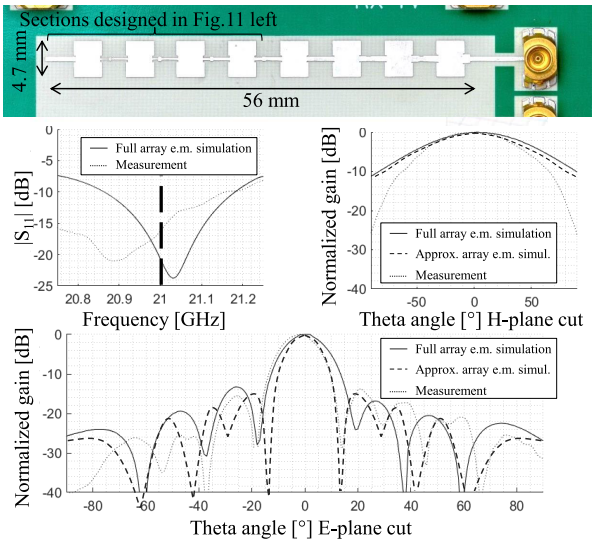

Fig. 12. Designed 8 × 1 array and its simulated and measured $|S_{11}|$ and normalized radiation pattern at 21 GHz.

allows to directly extend the array by adding more sections without redesigning the previous ones. This is possible due to the fact that the only dependence on the number of elements (N) lies in the operating power gain, but (5) actually depends only section counted backward from the terminal one.

To prove this simplification, an $N = 8 \times 1$ array at 21 GHz has been addressed. The four terminal sections, in fact, require exactly the same power gain as the design of Section V-A5, and thus, the whole 4 × 1 array can be reused. Furthermore, four elements $n = 4$ to 1, corresponding to $m = 4$ to 7, are appended at the input. The contours of the G_P surface are the remaining ones in Fig. 4, along which the following pairs have been chosen: $z_I^{(N-4)} = 1.05$, $\phi_I^{(N-4)} = 73.8°$; $z_I^{(N-5)} = 0.89$, $\phi_I^{(N-5)} = 42°$; $z_I^{(N-6)} = 0.77$, $\phi_I^{(N-6)} = 49.3°$; $z_I^{(N-7)} = 0.63$, and $\phi_I^{(N-7)} = 51°$. Again, formulas to compensate the reactive effects of width discontinuities in microstrip have been applied to create the final layout. The result is shown in Fig. 12, as modeled in Ansys Electronics Desktop HFSS and as manufactured without any optimization.

The simulation confirms that the synthesis outcome is successful, with a very good matching at 21.04 GHz; measurements instead show the best return loss at 20.85 GHz and

a still acceptable level even down to 20.5 GHz, whereas the simulated $|S_{11}|$ curve already reaches -7 dB at 20.75 GHz.

The H-plane radiation pattern is very smooth, although measurements show a steeper decay beyond 55°; the measured E-plane radiation pattern follows very well the one simulated as approximate array, although with an asymmetry due to the protruding connector and feeding cable on one side, neglected by both simulations. The sidelobe levels also coincide reasonably well with the approximate array simulation (using ideal uniform illumination from an array of decoupled patches), thus implying that the designed network indeed provides a good uniform and in-phase illumination from all sections. The simulated gain is between 13.2 and 13.4 dBi in the full electromagnetic simulation and in the approximate array one, but unfortunately no gain measurement has been possible in the allotted timeframe for the characterization setup. Again, the agreement between measurements and expected results is rather good, and the design has been carried out merely by extending the 4×1 array without any redesign.

For comparison, a traditional inline 8×1 array of resonating elements would require halving the radiation resistance of each with respect to an already-designed 4×1 array, thus needing further simulations or an analytical equivalent model.

C. 5 × 1 Butterfly Patch Array at 31 GHz From [8]

The example provided in [8] involves a core element whose power gain surface reaches only $G_P = -5$ dB, which is insufficient for a terminal section: that paper, thus, implements a shift of the reference plane of the core element in the terminal section. In light of the bounds described in Section III-A, that modification is now explainable: the computation of the analytical maxima and minima for gain via (21) yields $0 < G_L^P < 0.898$ (compatible with an ideal terminal section) but achieving a very low gain requires unacceptably impedances for $z_I^{(N)}$: (20) for $G_P^N = -15$ dB, in fact, returns 160 or 20.4 Ω. The suggested countermeasure of adding a phase delay to port 1, thus, is the only choice: a $\phi_1^N = -30°$ section could be removed here, which brings the required input impedance to an acceptable value [about 110 Ω, confirmed by (20)].

For the other sections, instead, this additional delay is not needed, as their original contours include acceptable impedances. Instead, another issue arises due to the realizability of the mapping phase shifters: most of the required contours for the nonterminal sections require extreme z_M values. The empirically proposed solution was to introduce an offset $(\phi_2^{(n)} - 30°)$ in port 2's reference plane of the core element in all the nonterminal sections. This phenomenon is correctly predicted by the boundary proposed here as (22), which follows the unrealizable (white) regions of [8, Fig. 5].

D. 4 × 1 Slotted Waveguide Array at 27.25 GHz

As further example of application of the proposed technique, a slotted waveguide example is described, designed for application in a fixed-wireless access base station. The radiating element is a 45°-slanted slot in the narrow wall of a WR28 waveguide (7.11 × 3.56 mm). The slot itself is not optimized: 1.8-mm wide and carved into the 0.2-mm-thick metal waveguide. With the required single electromagnetic simulation of the core element, its scattering parameters are obtained at 27.25 GHz, as reported in Fig. 13.

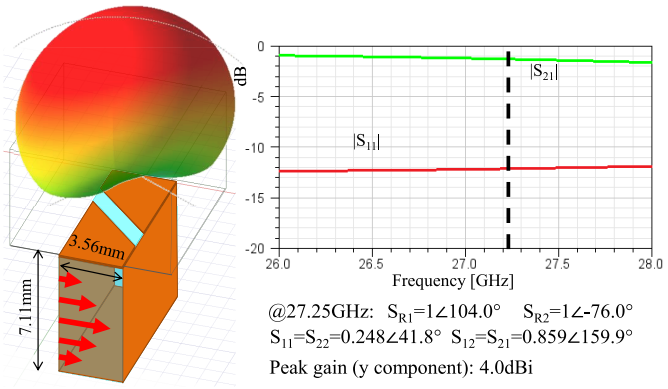

Fig. 13. Core element as narrow-wall slot in WR28 waveguide and its simulated scattering parameters and radiation characteristics at 27.25 GHz.

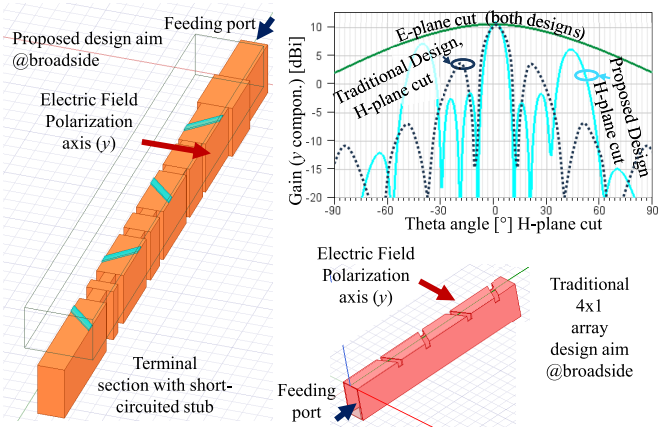

Fig. 14. 4×1 array designed for maximum radiation in broadside direction with linear polarization along y and corresponding traditional design. Simulated radiation patterns at 25.5 GHz are shown on the top right.

The scattering parameters are provided as input to the procedure in Section IV in order to design a four-element antenna array with electric field along the transversal direction, y.

The resulting cascade of phase shifters is then converted to waveguide, where the narrow-wall height is modulated according to the required impedances. Based on the reactive effects of such discontinuities, an analytical compensation is applied to embed them into equivalent phase shifters, which are then implemented by actual waveguide sections.

The final design is 50-mm long, as shown in Fig. 14, where the terminal section is closed by a short-circuited stub; the spacing between elements is about one wavelength, and slots are reversed to provide the correct constructive superposition along the desired polarization axis. The magnitude of S_{11} is also very good at the design frequency, being less than -25 dB, implying that the impedance-matching objective was reached. From basic array theory, the expected gain is expected 6 dB above the core element, thus 10 dBi, which is reasonably close to the simulated value (without losses) of 10.5 dBi.

For comparison purposes, a traditional design has also been carried out to obtain radiation in broadside direction, also

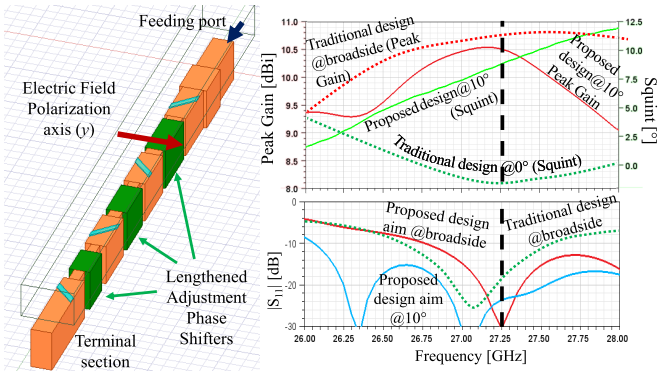

Fig. 15. 4×1 array designed for maximum radiation toward 10° with linear polarization along y, and peak gain-versus-frequency behavior and S_{11} response versus frequency. As reference, the simulated behaviors of the traditional design aiming in broadside (visible in Fig. 14) are also shown. The only elements changed with respect to the one aiming in broadside are the adjustment phase shifters, highlighted in green.

shown in Fig. 14, because of the available equivalent model developed ad hoc (see [19] and following works) constituted by a simple resonator. Half-wavelength sections are used to have many such resonators in parallel and radiating in phase, and thus, the resonator must be properly chosen depending on the number of elements of the array. The overall footprint of the traditional design is smaller (42 mm) because of the reduced spacing, and its peak gain is about 10.7 dBi. On the other hand, the closeby sidelobes are lower for the proposed array, while the sidelobes at 40° are lower in the traditional design.

To verify the changes to aim in nonbroadside direction, the array visible in Fig. 14 (left) can easily be modified. Only the adjustment phase shifters are affected, and their lengthening can be computed analytically, so that the maximum radiation occurs at 10°, as reported in Fig. 15.

The return loss of the array designed at 10° is also better than 20 dB at the design frequency, and the squint graph confirms that the peak gain of 10.5 dBi occurs slightly above 9°. The squint of the traditional design is limited, from $-1°$ to $+3°$, whereas the proposed design (designed at 10°) has a larger squint, from $+1.8°$ to $+12°$. No folding of the phase shifters has been leveraged in this example, which justifies the larger footprint and the increased squint in frequency. This example confirms the simple adjustment needed to steer the proposed array, whereas the traditional array design would need complete redesign, since altering the electrical delays between elements would also detrimentally affect the needed transformations for impedance matching.

VI. Conclusion

The method outlined here discusses a technique for the design of inline antenna arrays requiring ideally only a single electromagnetic simulation. It relies on a single core network, which must be properly simulated in its scattering and radiation characteristics. These are then manipulated by means of analytical formulae to compose the complete array by interposing phase shifters. Every section of the array is designed basically independently of the other stages.

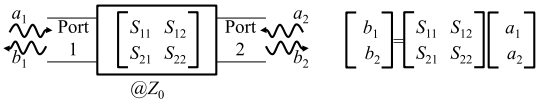

Fig. 16. Scattering parameters definition for arbitrary network.

Although the synthesis works at a single frequency, the obtained array can constitute a good starting point for later wideband optimizations. Due to intrinsic limitations, which may arise due to the chosen core network, the design flow may fail at some stage, but simple modifications can overcome them. The method moreover allows to accommodate different core sections along the array, if needed, and different impedance-transformation networks, such as stubs.

Two prototypes have been designed and manufactured without any optimization, and measurements confirm the expected behavior. Specific limitations emerged in a previously manufactured sample have also been justified. An additional example in slotted waveguide has been provided, to validate the procedure and also show the easy modification necessary to aim the array not in broadside.

Appendix I
Derivations

For easy reference, some of the relations used in this work are derived in this appendix. Scattering parameters of an arbitrary 2-port network are defined, as shown in Fig. 16, referred to an impedance Z_0. When an arbitrary load, expressed as reflection coefficient Γ_L referred to the same impedance Z_0, terminates port 2, the reflection coefficient observed looking into port 1 is obtained by eliminating variables a_2 and b_2 replacing $\Gamma_L = a_2/b_2$. The result is used, for instance, in (2).

Scattering parameters referred to impedance Z_0 corresponding to a phase shifter with phase delay ϕ and its own characteristic impedance Z_p can be computed starting from the scattering parameters referred to Z_p: $S_{11,Zp} = S_{22,Zp} = 0$ and $S_{21,Zp} = S_{12,Zp} = e^{-j\phi}$. These are then transformed by a change of reference impedance [20], from Z_p to Z_0 [defining $\Gamma = (Z_0 - Z_p)/(Z_0 + Z_p)$]

$$\begin{bmatrix} S_{11} & S_{12} \\ S_{21} & S_{22} \end{bmatrix} = \begin{bmatrix} S_{11,Zp} - \Gamma & S_{12,Zp} \\ S_{21,Zp} & S_{22,Zp} - \Gamma \end{bmatrix} \cdot \left(\begin{bmatrix} 1 - \Gamma S_{11,Zp} & -\Gamma S_{12,Zp} \\ -\Gamma S_{21,Zp} & 1 - \Gamma S_{22,Zp} \end{bmatrix} \right)^{-1}. \quad (23)$$

The result is found in Fig. 3 (top).

When two reciprocal 2-port networks A and B are cascaded by joining port 2 of network A with port 1 of network B, their Z_0-referred scattering matrices $\underline{\underline{S_A}}$ and $\underline{\underline{S_B}}$ can be converted to chain matrices $\underline{\underline{T_A}}$ and $\underline{\underline{T_B}}$, according to [20]. The overall chain matrix is then $\underline{\underline{T}} = \underline{\underline{T_A}}\,\underline{\underline{T_B}}$, which is finally converted back to the overall Z_0-referred scattering matrix $\underline{\underline{S}}$

$$\underline{\underline{S}} = \begin{bmatrix} S_{11A} - S_{11B}\Delta_A & S_{21A}S_{21B} \\ S_{21A}S_{21B} & S_{22B} - S_{22A}\Delta_B \end{bmatrix} \frac{1}{1 - S_{11B}S_{22A}}. \quad (24)$$

This result is used in (3), (8), and (16) to expand the scattering parameters $\underline{\underline{S}}^{IC}$ of the cascade of the input phase shifter and of the core section and also in (15) to cascade the mapping and adjustment sections as well ($\underline{\underline{S}}^{ICMA}$).

APPENDIX II
NONUNIFORM ILLUMINATION

In case of nonuniform array illumination, the power gain of each section can be obtained by elaborating the expression of illumination and power gain

$$I^{(n)} = \frac{\text{Power radiated by section } n}{\text{Power accepted by section 1}} \quad \text{with} \quad 1 = \sum_{n=1,\ldots,N} I^{(n)} \tag{25}$$

$$G_P^{(n)} = \frac{\text{Power forwarded to section } (n+1)}{\text{Power absorbed by section } n}. \tag{26}$$

Moreover, assuming that the input, mapping, and adjustment shifters are lossless

$$\text{Pow. abs. by sect. } n = \text{Pow. rad. by sect. } n + \text{Pow. fwd. to sect. } (n+1). \tag{27}$$

Therefore, for element n, it becomes

$$I^{(n)} \frac{\text{Pow. acc. by sect. 1}}{\text{Pow. acc. by sect. } n} + G_P^{(n)} = 1 \tag{28}$$

yielding the following expressions.

1) $n = 1$ (first element of the array): $G_P^{(1)} = 1 - I^{(1)}$.
2) $n = 2$: $G_P^{(1)} = 1 - \frac{I^{(2)}}{1-I^{(1)}}$.
3) Generical element n: $G_P^{(n)} = 1 - \frac{I^{(n)}}{\prod_{i<n} G_P^{(i)}}$.
4) $n = N$ (terminal element): $G_P^{(N)} = 1 - \frac{I^{(N)}}{\prod_{i<N} G_P^{(i)}} = 0$.

The case of uniform illumination can be easily obtained from this general expression by setting $I^{(n)} = 1/N$, yielding the expressions for power gain given in Section II-C.

Nonuniform illumination is often used for sidelobe reduction, null placement, and beam shaping but also when mutual-coupling compensation techniques are used, i.e., [9].

It is worth mentioning that the technique described here privileges using one single-core radiating element, thus requiring only one electromagnetic simulation, while computing complex interconnecting structures (three phase shifters for each section: input, mapping, and adjustment) even for nonuniform illumination. Most techniques for nonuniform illumination instead privilege simple interconnections while requiring different radiating elements along the line (usually smaller radiators toward the edge and half-wavelength connection lines). For this approach, either an analytical or empirical model must, however, be available, often requiring numerous electromagnetic simulations. The designer can, thus, weigh the two approaches to determine which one best fits the case at hand. Hybrid techniques can also be devised, leveraging two or three different core elements, provided, respectively, as initial, central, and terminal sections to the technique proposed in this manuscript, adding the benefits of both methods: no actual modeling required, no extensive simulations, and no extreme impedance values in the interconnecting lines.

REFERENCES

[1] A. Abdulkhaleq et al., "Energy-efficient RF for UDNs," in *Energy-Efficient RF for UDNs*. Cham, Switzerland: Springer, 2022, pp. 123–166.

[2] R. C. Hansen, *Phased Array Antennas*. Hoboken, NJ, USA: Wiley, 2009, pp. 164–189.

[3] R. J. Mailloux, *Phased Array Antenna Handbook*, 2nd ed. London U.K.: Artech House, 2006, vol. 110.

[4] T. A. Milligan, *Modern Antenna Design*, 2nd ed. Hoboken, NJ, USA: Wiley, 2005.

[5] R. Chopra and G. Kumar, "Series- and corner-fed planar microstrip antenna arrays," *IEEE Trans. Antennas Propag.*, vol. 67, no. 9, pp. 5982–5990, Sep. 2019.

[6] R. A. Sainati, *CAD of Microstrip Antennas for Wireless Applications*. Boston, MA, USA: Artech House, 1996.

[7] T. Yuan, N. Yuan, and L.-W. Li, "A novel series-fed taper antenna array design," *IEEE Antennas Wireless Propag. Lett.*, vol. 7, pp. 362–365, 2008.

[8] M. Oldoni, S. Moscato, S. C. Mejllones, and C. Franceschet, "Direct analytical synthesis of broadside inline antenna arrays," in *Proc. 52nd Eur. Microw. Conf. (EuMC)*, Milan, Italy, Sep. 2022, pp. 672–675.

[9] S. Lee and S. Choi, "Universal and non-iterative design method for in-phase radiation of microstrip traveling-wave series-fed antenna arrays," *IEEE Trans. Antennas Propag.*, vol. 71, no. 2, pp. 1403–1413, Feb. 2023.

[10] C. Balanis, *Antenna Theory: Analysis and Design*, 2nd Ed. Hoboken, NJ, USA: Wiley, 1982.

[11] C. L. Dolph, "A current distribution for broadside arrays which optimizes the relationship between beam width and side-lobe level," *Proc. IRE*, vol. 34, no. 6, pp. 335–348, Jun. 1946.

[12] S. A. Schelkunoff, "A mathematical theory of linear arrays," *Bell Syst. Tech. J.*, vol. 22, no. 1, pp. 80–107, Jan. 1943.

[13] H. J. Orchard, R. S. Elliott, and G. J. Stern, "Optimising the synthesis of shaped beam antenna patterns," *IEE Proc. H*, vol. 132, pp. 63–68, Feb. 1985.

[14] E. Botha and F. Ares, "Extension of the orchard-elliott synthesis method to pure real non-symmetrical shaped patterns," in *Proc. IEEE Antennas Propag. Soc. Int. Symp. Dig.*, Jul. 1997, pp. 2260–2263.

[15] D. Pozar, *Microwave Engineering*, 4th ed. Hoboken, NJ, USA: Wiley, 2011, ch. 12.

[16] J. Yin, Q. Wu, C. Yu, H. Wang, and W. Hong, "Low-sidelobe-level series-fed microstrip antenna array of unequal interelement spacing," *IEEE Antennas Wireless Propag. Lett.*, vol. 16, pp. 1695–1698, 2017.

[17] M. Li, Z. Zhang, M.-C. Tang, D. Yi, and R. W. Ziolkowski, "Compact series-fed microstrip patch arrays excited with Dolph–Chebyshev distributions realized with slow wave transmission line feed networks," *IEEE Trans. Antennas Propag.*, vol. 68, no. 12, pp. 7905–7915, Dec. 2020.

[18] A. Tugulea and I. R. Ciric, "Equivalent circuit for a microstrip step discontinuity," in *Proc. Symp. Antenna Technol. Appl. Electromagn.*, Jul. 2000, pp. 261–264.

[19] A. Oliner, "The impedance propeties of narrow radiating slots in the broad face of rectangular waveguide: Comparison with measurement," *IRE Trans. Antennas Propag.*, vol. 5, no. 1, pp. 12–20, Jan. 1957.

[20] M. Steer, *Microwave and RF Design, Networks*, vol. 3. Chapel Hill, NC, USA: Univ. North Carolina Press, 2019, ch. 2.

Matteo Oldoni (Member, IEEE) was born in Milan, Italy, in 1984. He received the Ph.D. degree in information technology from the Politecnico di Milano, Milan, in 2013.

He has worked as a Microwave Designer with the Passive Microwave Components Laboratory, SIAE Microelettronica, Milan, becoming a Technical Staff Member, and cooperated with several companies and research institutions internationally. Since June 2022, he has been a full-time Researcher at the Electronics, Information and Bioengineering Department, Politecnico di Milano. His research interests include synthesis and design techniques for microwave filters, algorithms development for computer-aided tuning, and antenna design.

Mr. Oldoni was a recipient of the Young Engineers Prize of the 39th European Microwave Conference.

Stefano Moscato was born in Pavia, Italy, in 1988. He received the Ph.D. degree in electronics engineering from the University of Pavia, Pavia, in 2016.

He was a Visiting Ph.D. Student at Georgia Tech, Atlanta, GA, USA, in early 2015. He became part of the Research and Development Microwave Group, SIAE Microelettronica, Milan, Italy, in May 2017. Since September 2022, he has been the head of the 1337 research and development group devoted to the design and validation of mm-wave passive components, antennas, and subsystems. He is involved in innovation programs and founded studies for microwave backhauling, O-RAN equipment, and space-oriented assemblies. He has authored more than 40 articles in international journals and conferences. His research activities have been focused on RF-to-mm-wave passive component.

Dr. Moscato was a recipient of the IEEE Microwave Theory and Technique Society (MTTS) Undergraduate/Pre-Graduate Scholarship in 2012. He was the Chair of the IEEE Student Branch, University of Pavia, from 2013 to 2016.

Steven Caicedo Mejillones received the Diploma degree in telematics engineering and the master's degree in telecommunications from the Escuela Superior Politecnica del Litoral (ESPOL), Guayaquil, Ecuador, in 2014 and 2017, respectively, and the Ph.D. degree in information technology from the Politecnico di Milano, Milan, Italy, in 2023.

From 2014 to 2018, he worked as a planning and optimization engineer for radio access networks (RANs) in several telecommunications companies in Ecuador, including the mobile operator Claro from the America Movil Group. From 2018 to 2021, he was an Early-Stage Researcher at SIAE Microelettronica, Milan, within the H2020 Marie-Curie ITN 5G STEP FWD Program. Since 2021, he has been a Microwave Designer for space, backhaul, and O-RAN applications at SIAE Microelettronica. His research interests include synthesis and design techniques for microwave filters, filtering antennas, and phased arrays.

Gian Guido Gentili (Member, IEEE) received the Laurea degree in electronics engineering from the Politecnico di Milano, Milan, Italy, in 1987.

In 1989, he joined the Dipartimento di Elettronica ed Informazione, National Research Council (CNR), Center for Space Telecommunications, Politecnico di Milano, as a Researcher. In 2001, he became a Senior CNR Researcher. He became an Associate Professor with the Politecnico di Milano in 2002. He was a Visiting Scholar at the Universidad Politecnica de Madrid, Madrid, Spain, in 1993 and 1995. He is responsible for the Electromagnetics Laboratory, Politecnico di Milano "Wavelab." His research interests include numerical method for electromagnetics, antennas and feed systems for terrestrial and space applications, microwave passive devices, filters, and plasmonics.

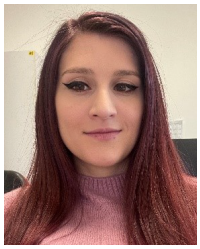

Cristina D'Asta was born in Italy in 1995. She received the M.Sc. degree in telecommunication engineering from the Politecnico di Milano, Milan, Italy, in 2020, where she is currently pursuing the Ph.D. degree in information technology with the Dipartimento di Elettronica, Informazione e Bioingegneria.

She has been collaborating with Huawei Technologies, Segrate (MI), Italy, in the framework of the Joint Research Center. Her research interests include synthesis and design of microwave filters, and innovative technologies for sub-THz passive devices and antennas.

Open Access funding provided by 'Politecnico di Milano' within the CRUI CARE Agreement